Nickel-copper graphene foam prepared by atmospheric pressure chemical vapour deposition for supercapacitor applications

M.J. Madito[a],*, K.S. Matshoba[b], F.U. Ochai-Ejeh[b], N. Mongwaketsi[a], C.B. Mtshali[a], M. Fabiane[b,c], N. Manyala[b]

[a]iThemba LABS, National Research Foundation, PO Box 722, Somerset West, 7129 Cape Town, South Africa
[b]Department of Physics, Institute of Applied Materials, SARCHI Chair in Carbon Technology and Materials, University of Pretoria, Pretoria 0028, South Africa
[c]Department of Physics, National University of Lesotho, P.O. Roma 180, Lesotho

*Corresponding author. mmadito@tlabs.ac.za

Highlights

• Ni-Cu graphene foam was prepared by atmospheric pressure CVD.
• Ni-Cu graphene foam displayed mainly monolayer and bilayer.
•The electrochemical properties of Ni-Cu graphene foam as a current collector were evaluated.
• Ni-Cu graphene foam current collector displayed a high electrochemical performance.

Abstract

This study reports on Ni and Ni-Cu graphene foam prepared by atmospheric pressure chemical vapour deposition. The Ni-Cu foam alloys were prepared using a three-dimensional (3D) scaffold template of polycrystalline nickel foam which is commonly used as a current collector in supercapacitor electrodes. The morphological, composition and structural characterization of as-grown Ni and Ni-Cu graphene foam were carried out using confocal Raman spectroscopy imaging, scanning electron microscopy (SEM), high-resolution transmission electron microscopy (HR-TEM), energy-dispersive X-ray spectrometer (EDS) and X-ray photoelectron spectroscopy (XPS). The results demonstrated that Ni-Cu graphene foam is mainly monolayer and bilayer as compared to Ni graphene foam which is typically a few-layer graphene. The electrochemical performance of Ni and Ni-Cu graphene foam as current collectors were evaluated in a three-electrode electrochemical cell using 1 M $NaSO_4$ aqueous electrolyte and porous activated carbon (AC) produced from lightweight material cork (*Quercus suber*) as the active electrode material. The AC on Ni-Cu graphene foam current collectors exhibited a high specific capacitance (250–300 F g^{-1} at 1 A g^{-1}) and good electrochemical stability (94–100% capacitance retention) over 6000 constant charge-discharge cycles at 5 A g^{-1}.

Keywords: Graphene foam; Ni foam; Ni-Cu alloy; CVD graphene; Current collector

1. Introduction

Supercapacitors (or electrochemical capacitors) have attracted considerable recent attention due to their high power density, fast dynamics of charge propagation, long cycle life performance (>10,000 cycles), low maintenance, safe and reliable performance, for energy

storage applications [1]. Also, supercapacitors have the potential to complement or eventually replace the rechargeable batteries for some energy storage applications. But, supercapacitors are plagued with a lower energy density (i.e. ~5–8 Wh kg^{-1}) as compared to rechargeable lithium-ion batteries (120–200 Wh kg^{-1}) [[2], [3], [4]]. Therefore, there are great research efforts towards enhancing the performance of supercapacitor devices to have considerable energy densities comparable to that of lithium-ion batteries. According to their charge storage mechanism, there are two types of supercapacitors, i.e. electrochemical double-layer capacitor (EDLC) and pseudocapacitor. EDLC stores charge electrostatically with the charged ion located at the surface of the electrode material. However, the charge storage mechanism of pseudocapacitors involves a fast redox reaction at the electrode-electrolyte interface [5,6]. Carbon-based materials have been mostly used as the electrode materials for EDLC due to their high specific surface area, good electrical conductivity and large pore size distribution (micro, *meso* and macropores) [7,8], while pseudocapacitors are from redox-active materials such as transition metal oxides or hydroxides and conductive polymers.

Hybrid materials or devices incorporating EDLC and pseudocapacitor materials are thought to give the next generation high-performance supercapacitor devices [9,10]. In hybrid supercapacitors, EDLC electrode materials are commonly used as negative electrodes and pseudocapacitive materials as positive electrodes to improve the overall energy storage capacitance of the supercapacitors. These materials are commonly coated on Ni foam current collector which is a low density permeable three-dimensional (3D) material with very high porosity [[11], [12], [13], [14], [15], [16], [17], [18], [19]]. A typical current collector for electrochemical energy storage systems should have high electrical conductivity, excellent chemical stability and potential window in electrolytes (to support the electrochemical stability window and the ionic conductivity of electrolytes), and good mechanical strength or flexibility. Ni foam has proved to be a good current collector in aqueous and organic/ionic liquids electrolytes (e.g. see most articles on the electrochemical performance of supercapacitors).

Previously, studies have prepared 3D graphene foam by a chemical vapour deposition (CVD) process using the Ni-foam template [20]. These 3D Ni graphene foam networks were used as templates for the synthesis of 3D graphene nanocomposites for high-performance supercapacitor electrodes [[21], [22], [23]]. A 3D Ni graphene foam framework advantageously serves as a 3D support of large capacity to uniformly anchor the transition metal oxides/hydroxides as well as electrically conductive polymers with well-defined size, shapes, and crystallinity for the enhanced electrochemical performance of the supercapacitor electrodes. Research efforts have been focused on improving the interactions between graphene foam and their composite materials to optimize the pseudocapacitance and further improve the performance of supercapacitors [[21], [22], [23]]. The interface between the collector and active electrode materials is also important since it controls the contact impedance of the electrodes. Besides, active materials directly grown on the current collectors have shown to have improved contact impedance [[21], [22], [23]]. Nonetheless, more effort is needed in designing current collectors, especially with reduced ohmic drops at the interface between active materials and current collectors for the enhanced electrochemical performance of the supercapacitors.

Herein, we report on atmospheric pressure AP-CVD synthesis of graphene on Ni and Ni-Cu foam substrates. Ni-Cu foam alloys were prepared using a 3D scaffold template of polycrystalline nickel foam which is commonly used as a current collector in supercapacitor electrodes. The characterization of as-grown Ni and Ni-Cu graphene foam was carried out

using confocal Raman spectroscopy imaging, scanning electron microscopy (SEM), energy-dispersive X-ray spectrometer (EDS) and X-ray photoelectron spectroscopy (XPS). The electrochemical properties of Ni and Ni-Cu graphene foam as current collectors were evaluated in the three-electrode electrochemical cell using an aqueous electrolyte. Based on the characterization results, Ni-Cu graphene foam displayed mainly monolayer and bilayer as compared to Ni graphene foam which is typically a few-layer graphene. The active electrode material (activated carbon) coated on Ni-Cu graphene foam current collectors displayed a higher electrochemical performance compared to electrode materials on Ni and Ni graphene foam current collectors.

2. Experimental details

2.1. Ni and Ni-Cu graphene foam synthesis

For Ni-Cu foam alloy preparation, 5 × 5 mm^2 pieces of Ni foam were cleaned by annealing at 1000 °C under Ar and H_2 at flow rates of 300 and 200 standard cubic centimeters per minute (sccm), respectively, for 30 min. A 3D scaffold template of polycrystalline nickel foam with an areal density of 420 g m^2 and a thickness of 1.6 mm was purchased from Alantum (Munich, Germany). 5 × 5 mm^2 pieces of Cu films were obtained from an annealed (99.8% purity) 25 μm thick copper foil purchased from Alfa Aesar. The Cu films were cleaned by immersing them in an aqueous nitric acid for 10 s, to get rid of impurities, and then washed with distilled water followed by an ultrasonic bath with isopropanol to remove the residues. Furthermore, a cleaned Cu film with a mass of 148 mg was pressed on 5 × 5 mm^2 piece of Ni foam with a mass of 837 mg, then annealed at a high temperature of 1140 °C (above the melting point of Cu, i.e. 1086 °C) under Ar flow (1000 sccm) for 10 min to melt and diffuse Cu in Ni foam surface, as illustrated in Scheme 1. After annealing the mass of the sample was equivalent to the total mass of Cu film plus Ni foam (987 mg), and this sample was referred to as Ni-15 mass% Cu foam alloy. Similarly, two cleaned 5 × 5 mm^2 pieces of Cu films with a total mass of 282 mg were pressed together, then on a piece of Ni foam with a mass of 837 mg and annealed at 1140 °C under Ar flow (1000 sccm) for 10 min to obtain Ni-25 mass% Cu foam alloy (Scheme 1).

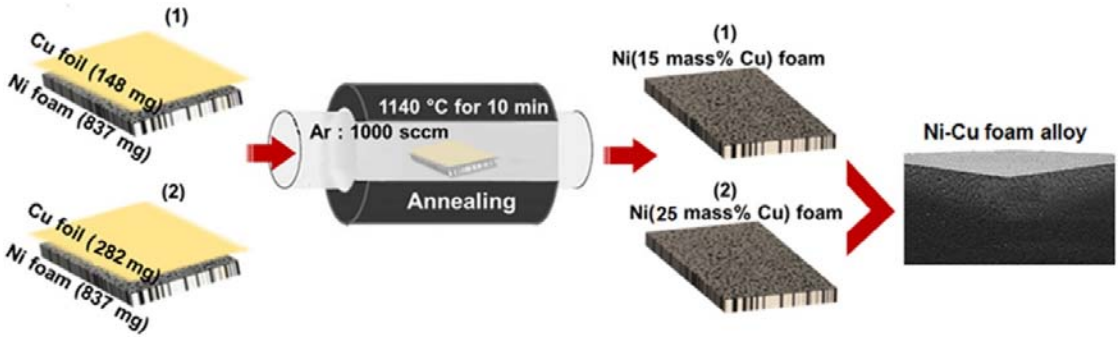

Scheme 1. Ni—Cu foam alloy preparation route.

Moreover, Ni, Ni-15 mass% Cu and Ni-25 mass% Cu foam substrates were placed at the centre of an AP-CVD quartz tube, then graphene growth was carried out at 1000 °C for 5 min using a mixture of gasses, Ar:H_2:CH_4 with flow rates of 300:9:10 sccm, respectively. Immediately after 5 min growth time, the CH_4 was stopped and the tube was pushed to a cooler region of the furnace to allow the samples to rapidly cool down to room temperature.

2.2. Morphological, composition and structural characterization of Ni and Ni-Cu graphene foam

The characterization of the as-grown Ni and Ni-Cu graphene foam samples was carried out using different techniques: Raman spectroscopy, scanning electron microscopy (SEM, Zeiss Ultra Plus 55 field emission scanning electron microscope operated at 2.0 kV), high-resolution transmission electron microscopy (HR-TEM, using a cold feld-emission JEOL F200 TEM operating at 200 kV), energy-dispersive X-ray spectrometer (EDS), and X-ray photoelectron spectroscopy (XPS, using a Thermo Fisher photoelectron spectrometer fitted with a monochromatic Al Kα radiation X-ray source). The Raman spectroscopy analysis/imaging was carried out using the WITec alpha300 RAS+ confocal Raman microscope. The analysis was carried out using a 50×/0.75*NA* objective and 532 nm laser at a power of 2 mW. The image scans were acquired over 25 × 25 μm^2 areas with 100 points per line and 100 lines per image using an integration time of 3 s. The image scans were obtained by scanning the sample under the laser spot using a piezo-scanner which is quite fast and very accurate. The diffraction-limited laser spot size is estimated by $\Delta x = 0.61 \times \lambda/NA$, where λ is the wavelength and *NA* is the numerical aperture of the objective used for analysis. Therefore, for 50×/0.75*NA* objective used in this work, the lateral resolution is about 433 nm. The spectral resolution is in the order of 1 cm^{-1}. WITec Project FIVE software was used for Raman image data processing.

2.3. Electrochemical characterization

Moreover, the as-grown Ni and Ni-Cu graphene foam samples were farther tested as current collectors in a three-electrode configuration using a Bio-Logic VMP300 potentiostat/ galvanostat workstation at room temperature. The electrodes were prepared by making a homogenous paste of 80 wt% active material (activated carbon (AC)), 10 wt% carbon black and 10 wt% polyvinyl difluoride (PVDF) binder with dropwise addition of *N*-methyl pyrrolidone (NMP) in an agate mortar. The paste was then coated on 1 × 1 cm^2 of Ni and Ni-15 mass% Cu foam, and graphene-coated Ni, Ni-15 mass% Cu and Ni-25 mass% Cu foam current collectors and dried in an oven at 60 °C overnight to ensure complete evaporation of the NMP. Thereafter, the masses of the coated active material (AC) on current collectors were 2.9 mg AC/Ni, 1.9 mg AC/Ni graphene foam, 2.4 mg AC/Ni-15 mass% Cu foam, 2.1 mg AC/Ni-15 mass% Cu graphene foam and 1.6 mg AC/Ni-25 mass% Cu graphene foam. Before three-electrode measurements, the active material was pressed onto the current collectors under a pressure of 30 MPa. The three-electrode measurements, i.e. cyclic voltammetry (CV), galvanostatic charge-discharge (GCD), and electrochemical impedance spectroscopy (EIS) were performed in 1 M $NaSO_4$ aqueous electrolyte with glassy carbon as the counter electrode and Ag/AgCl as a reference electrode. The measurements were carried out in the negative potential window (−0.8–0.0 V vs. Ag/AgCl). The EIS was performed over a frequency range of 10 mHz to 100 kHz in an open circuit potential. A porous AC used in this work was produced from cheap and lightweight material cork (*Quercus suber*), a spongy material that comes from the bark of an evergreen oak tree. This AC was synthesized and fully characterized and tested for supercapacitor applications in our previous work [11,12].

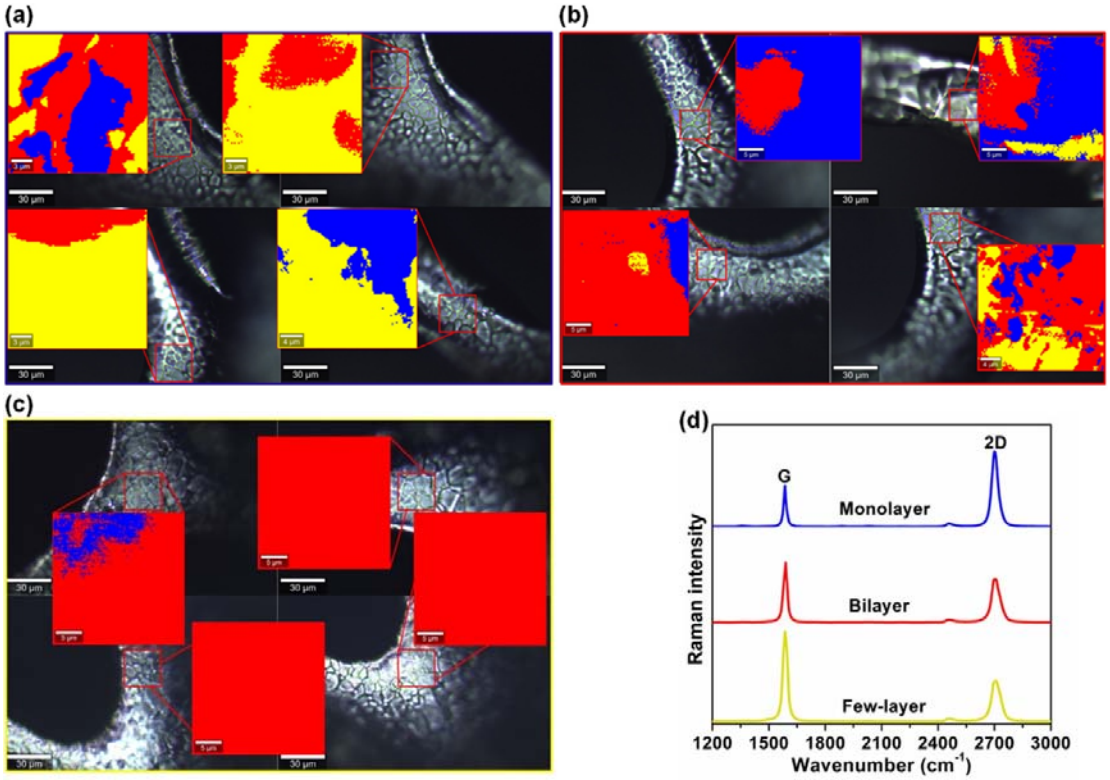

Fig. 1. The optical microscope images with an overlay cluster analysis images of different parts of the samples: (a) Ni graphene foam, (b) Ni-15 mass% Cu graphene foam, (c) Ni-25 mass% Cu graphene foam, and (d) the corresponding cluster average spectra (each spectrum-color correspond to the cluster image area of the same color in (a–c)).

3. Results and discussion

3.1. Morphological, composition and structural characterization of Ni and Ni-Cu graphene foam

3.1.1. Raman spectroscopy imaging

The quality and the number of layers of as-grown Ni and Ni-Cu graphene foam were evaluated using confocal Raman imaging. Because of the irregular surface of the Ni foam, the laser beam with a spot size of ~433 nm was scanned over a focused area (25 × 25 μm^2) to avoid a variation in the detected signal counts. Besides, a large area (>50 μm^2) of the irregular surface of Ni foam could be scanned using the True Surface Imaging mode which keeps the true surface of the sample in constant focus during the entire measurement procedure. Fig. 1 shows the Raman imaging data of as-grown Ni and Ni-Cu graphene foam. Fig. 1(a) to (c) displays the overlay cluster analysis images on the optical microscope images of different parts of the samples, and the corresponding cluster average spectra are presented in Fig. 1(d). These Raman spectra reveal that the as-grown Ni and Ni-Cu graphene foam have a non-uniform thickness, i.e. monolayer, bilayer and few-layer graphene. Briefly, in the Raman data processing tool of WITec Project FIVE software, the cluster analysis of the acquired Raman image data set automatically finds similar spectra in an image spectrum data set and creates the cluster distribution maps and the corresponding cluster average spectra. It can be seen in cluster images of Fig. 1(a), that Ni graphene foam has non-uniform thickness

with dominating few-layer graphene. On the contrary, Ni-15 mass% Cu graphene foam (Fig. 1(b)) displays less few-layer graphene with dominating mono and bilayer graphene compared to Ni graphene foam while Ni-25 mass% Cu graphene foam showed almost only bilayer graphene (Fig. 1(c)). In Fig. 1(d), the absence of the D-band in the Raman spectra shows high-quality as-grown graphene since the presence of D-band demonstrates defects in the translational symmetry of the graphene lattice [24,25].

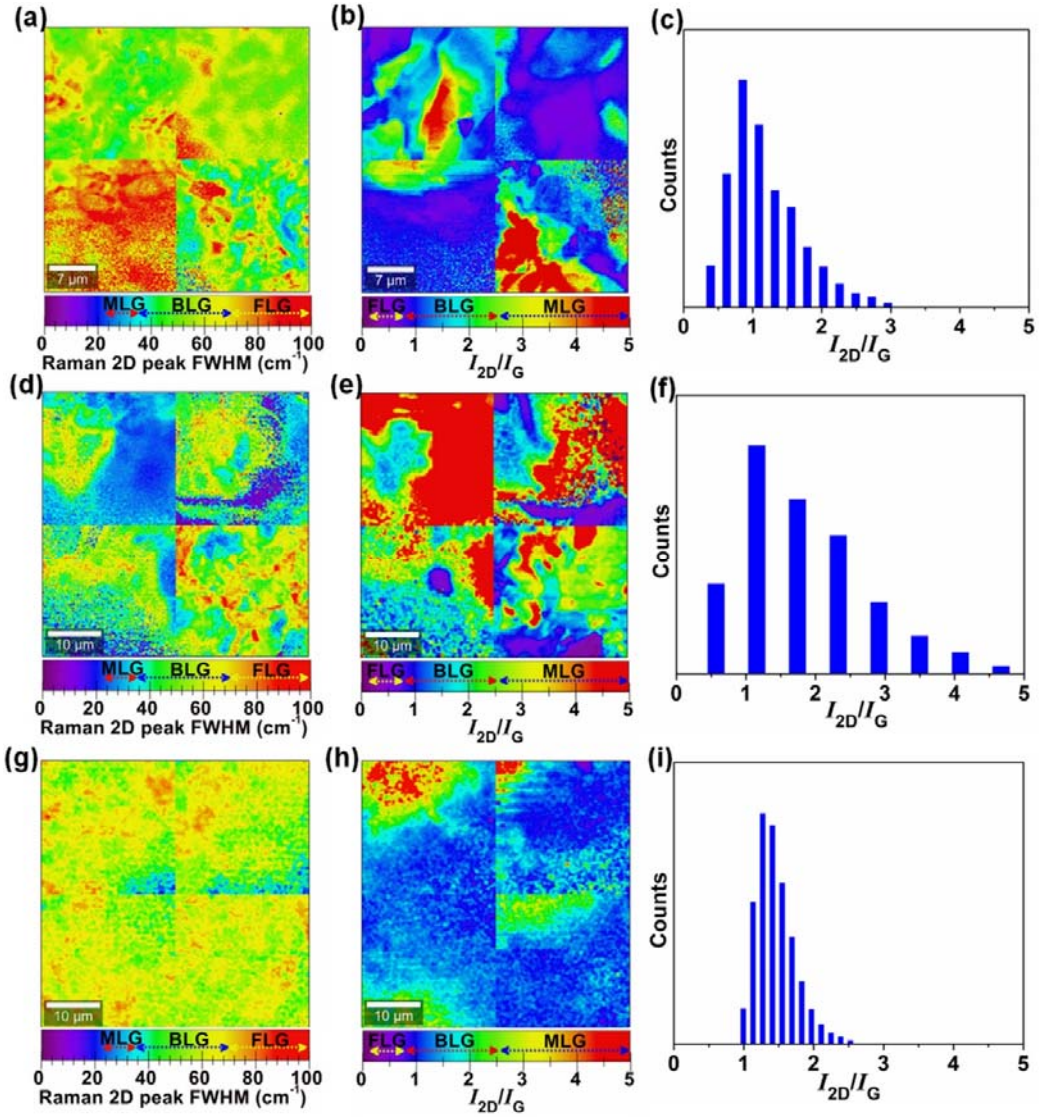

Fig. 2. The mapping of 2D peaks FWHMs and I_{2D}/I_G ratios and the corresponding distribution of the I_{2D}/I_G ratios of the Raman data set of: (a–c) Ni graphene foam, (d–f) Ni-15 mass% Cu graphene foam, and (g–i) Ni-25 mass% Cu graphene foam.

Moreover, the analysed areas of each sample, as shown in Fig. 1, were stitched together in the mapping of 2D peaks Full width at half maximum (FWHM) and the corresponding 2D-to-G peaks intensities ratio (I_{2D}/I_G), as presented in Fig. 2. The 2D peaks FWHMs in the range of 26–38 cm^{-1} and I_{2D}/I_G ratios in the range of ~2.5–4.5 are attributed to monolayer graphene (MLG). In addition, the FWHMs is in the range of 39–70 cm^{-1} and I_{2D}/I_G ratios in the range of 0.7–2.2 are attributed to bilayer graphene (BLG) [26,27], while for Few-layer graphene

(FLG) the distribution of the FWHMs is >70 cm^{-1} and $I_{2D}/I_G < 1$. Fig. 2(a–c) presents the graphene features of Ni graphene foam which show mainly FLG ($I_{2D}/I_G < 1$). In Ni graphene foam, the 2D peaks FWHMs underestimate the number of layers because of random (non-Bernal) stacking of graphene which yields 2D peaks FWHMs close to those of MLG (~40 cm^{-1}). Ni typically grows non-uniform FLG graphene with a significant fraction of non-Bernal stacking. Fig. 2(d–f) presents the graphene features of Ni-15 mass% Cu graphene foam which shows dominating MLG and BLG and displays less FLG compared to Ni graphene foam. This is mainly due to Cu in Ni-Cu alloy which has a very low decomposition rate of CH_4 compared to Ni, therefore, it reduced an amount of decomposed carbon which materialized into graphene. A further increase in Cu content in Ni foam (Ni-25 mass% Cu graphene foam) showed only a fraction of MLG and mainly BLG (Fig. 2(g–i)). This is in agreement with previously published results on CVD graphene growth on Cu-Ni alloy substrates which demonstrated a preferential growth of Bernal stacked bilayer graphene [26,28,29].

3.1.2. SEM and HRTEM

The surface morphologies of the Ni, Ni-15 mass% Cu and Ni-25 mass% Cu graphene foam samples were examined using SEM (Fig. 3). Fig. 3(a) presents an SEM image of the Ni foam without graphene at low (inset figure) and high magnification which shows a smooth surface. On the contrary to Ni foam smooth surface, Ni (Fig. 3(b)), Ni-15 mass% Cu (Fig. 3(c)) and Ni-25 mass% Cu (Fig. 3(d)) graphene foam displays wrinkles and ripples which could be attributed to the differences in thermal expansion coefficients between graphene and the metal substrates [30]. Furthermore, the surface of Ni-Cu alloy (i.e. before graphene growth, inset of Fig. 3(d)) appears different from that of Ni foam (inset of Fig. 3(a)) mainly because of the Cu foil which was first melted and, then diffused in Ni foam surface. Moreover, the surface morphology of Ni-25 mass% Cu graphene foam at the backside of the sample (Fig. 3(e), without Cu) appears similar to that of Ni graphene foam. This demonstrates the effect of a Ni-Cu gradient alloy. The 3D porous structure of Ni foam was maintained in both Ni and Ni-Cu graphene foam, as shown by Fig. 3(b) and (e) inset figures, respectively. Fig. 3(f) displays a typical HRTEM image of graphene foam after etching away the nickel template which shows a selected area electron diffraction (SAED) pattern (inset figure) similar to that of a few-layer graphene with a *d*-spacing of ~0.123 and 0.213 nm corresponding to Miller-Bravais indices (1−210) outer ring and (1−110), respectively [31].

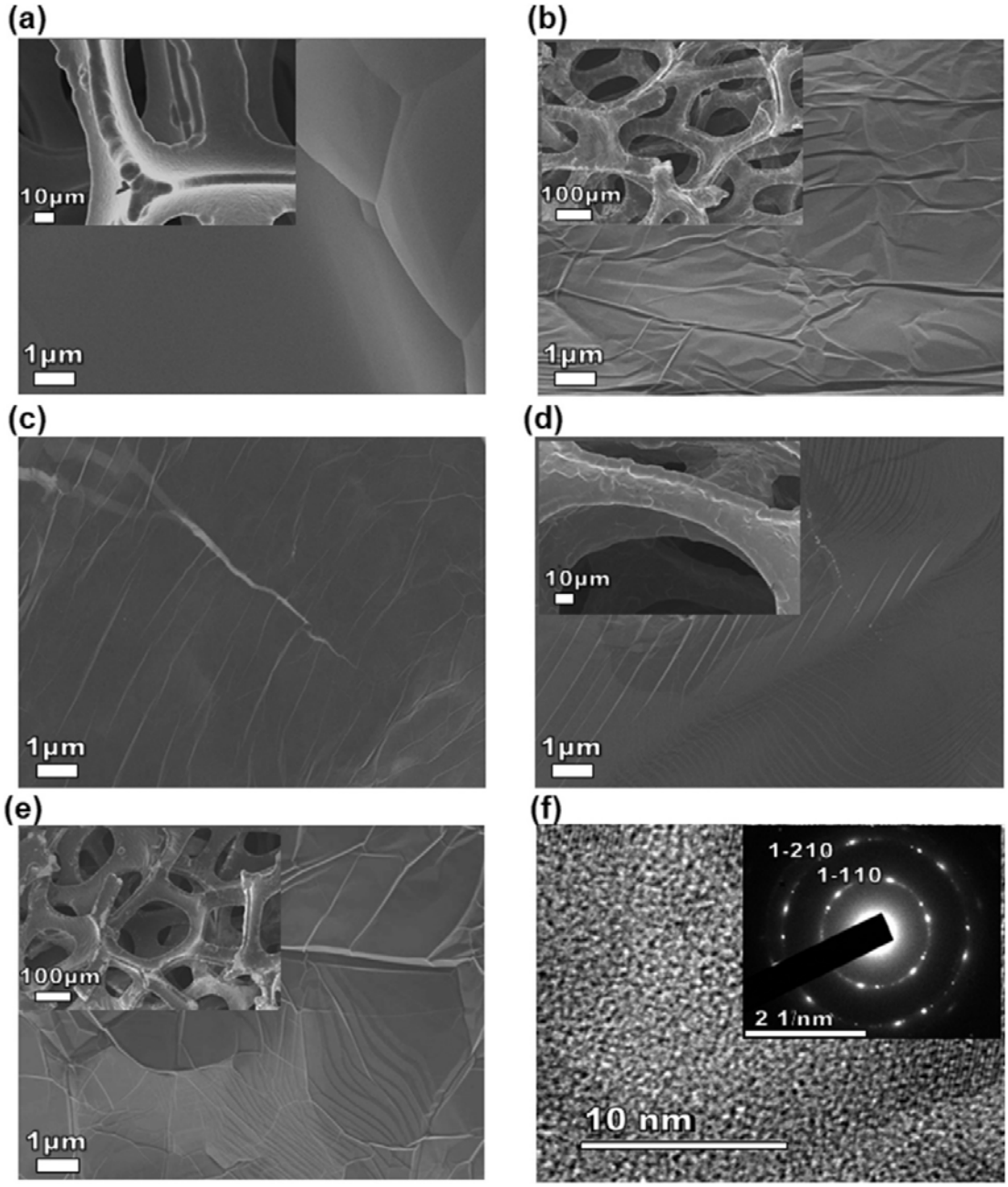

Fig. 3. SEM images: (a) Ni foam (inset: low magnification image), (b) Ni graphene foam, (c) Ni-15 mass% Cu graphene foam, (d) Ni-25 mass% Cu graphene foam, and (e) the backside (without Cu) of Ni-25 mass% Cu graphene foam (inset figures are low magnification SEM images). (f) The HRTEM image of graphene foam after etching away the nickel template and the corresponding selected area electron diffraction pattern (inset figure).

3.1.3. EDS and XPS

Moreover, the elemental composition of the as-grown Ni and Ni-25 mass% Cu graphene foam were obtained using EDS, as shown in Fig. 4. It can be seen from this figure that a high bulk content of carbon is dramatically reduced in Ni-Cu foam alloy as compared to Ni

graphene foam. This is primarily due to the lowered CH_4 decomposition rate of Ni by Cu since it has a very low CH_4 decomposition rate compared to Ni.

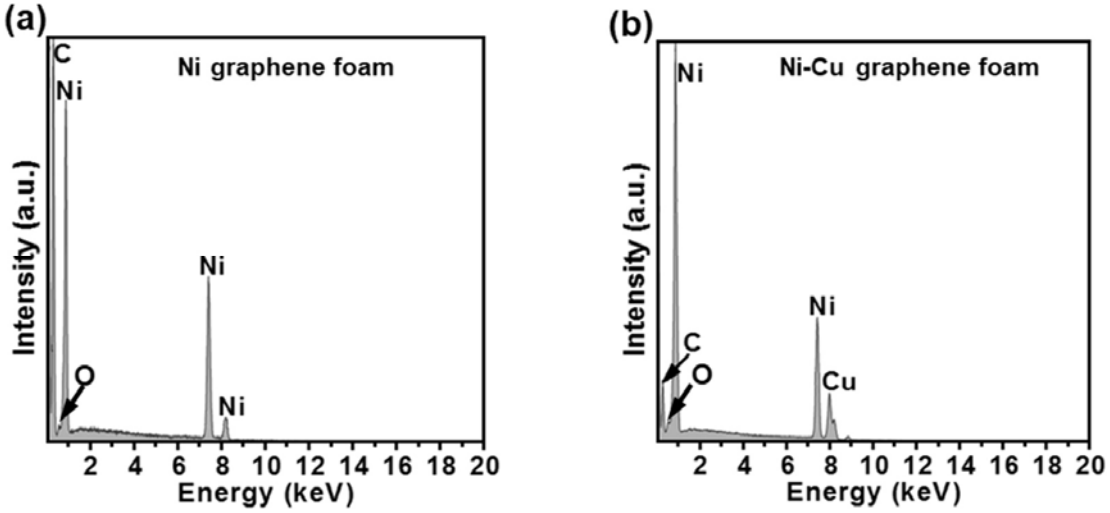

Fig. 4. EDS data: (a) Ni graphene foam, and (b) Ni-25 mass% Cu graphene foam.

Fig. 5, Fig. 6 show the XPS analysis of the as-grown graphene foam samples. Fig. 5 presents the wide scan XPS spectra of (a) Ni graphene foam, (b) Ni-15 mass% Cu graphene foam and Ni-25 mass% Cu graphene foam (c) topside and (d) backside, and the corresponding elemental compositions are shown in Table 1. The Ni graphene foam sample displays high carbon content as compared to Ni-Cu graphene foam samples, as expected. The XPS spectra of Ni-Cu graphene foam display C, Ni, Cu and O present in the samples. Furthermore, the backside of Ni-25 mass% Cu graphene foam does not show Cu hence it displays high carbon content similar to Ni graphene foam. It is also observed that a Ni-Cu alloy prepared with less Cu has less oxygen content, e.g. a Ni-15 mass% Cu graphene foam had about 6.3 at.% oxygen compared to Ni-25 mass% Cu graphene foam with 29.2 at.% (Table 1). This high oxygen content could be from an oxide layer residue after cleaning Cu films by immersing them in aqueous nitric acid and non-vacuum annealing of Ni-Cu at a high temperature of 1140 °C (to melt Cu foil and form a Ni-Cu alloy). Therefore, this could be avoided by depositing and annealing Cu film on Ni foam under a high vacuum chamber. Moreover, the C 1s core level spectrum of Ni graphene foam (Fig. 6(a)) shows the strongest peak of sp^2 C═C at 284.8 eV which indicates a graphene component, and the low-intensity oxide constituent, C−O at 286.3 eV. The O 1s core-level spectrum of Ni graphene foam (Fig. 6(c)) further confirms the oxide constituents present in the surface of the sample. In O 1s spectrum, a peak at 530.1 eV is attributed to the metal oxides (i.e. the ionization characteristics of oxygen species integrated in the material as OH^- or O_2^{2-} [32]), and the O 1s peaks at 531.9 and 533.1 eV are ionization associated with weakly adsorbed organic species [32]. Similar to Ni graphene foam, the C 1s core level spectrum of Ni-25 mass% Cu graphene foam (Fig. 6(d)) shows the strongest peak of sp^2 C═C (graphene component) and low-intensity oxide constituents. The Ni 2p and Cu 2p core-level spectra (Fig. 6(e) and (f)) confirm the Ni and Cu metal and a fraction of Ni- and Cu-oxides constituents present in the surface of the sample. The metal oxides are also confirmed by O 1s peak at 530.1 eV (Fig. 6(g)).

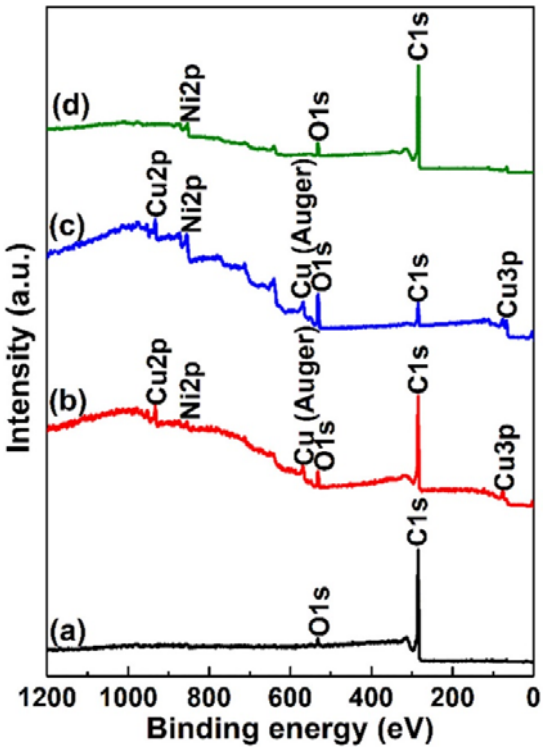

Fig. 5. Wide scan XPS spectra of (a) Ni graphene foam, (b) Ni-15 mass% Cu graphene foam and Ni-25 mass% Cu graphene foam (c) topside and (d) backside.

Table 1. XPS relative fractional concentrations of elemental compositions of Ni, Ni-15 mass% Cu and Ni-25 mass% Cu graphene foam.

Peaks position (eV)	Ni graphene foam	Ni-15 mass% Cu graphene foam	Ni-25 mass% Cu graphene foam	
	(at.%)	(at.%)	(at.%) (topside)	(at.%) (backside)
284.8 (C 1s)	97.3	90.4	50.4	92.5
531.3 (O 1s)	1.8	6.3	29.2	5.5
853.7 (Ni 2p)	0.9	1.3	14.2	2.0
933.2 (Cu 2p)	–	2.0	6.2	–

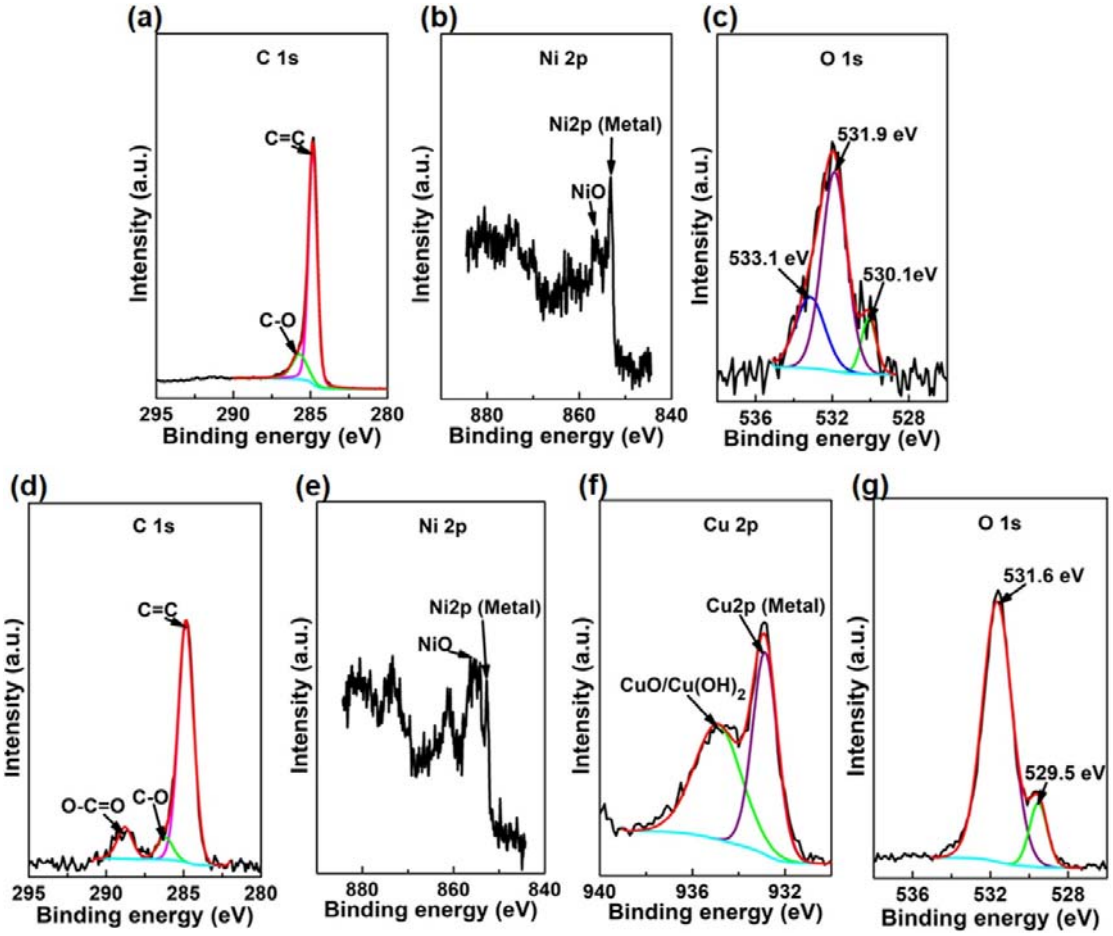

Fig. 6. XPS core level spectra: (a) C 1s, (b) Ni 2p and (c) O 1s spectra of Ni graphene foam. (d) C 1s, (e) Ni 2p, (e) Cu 2p and (c) O 1s spectra of Ni-25 mass% Cu graphene foam.

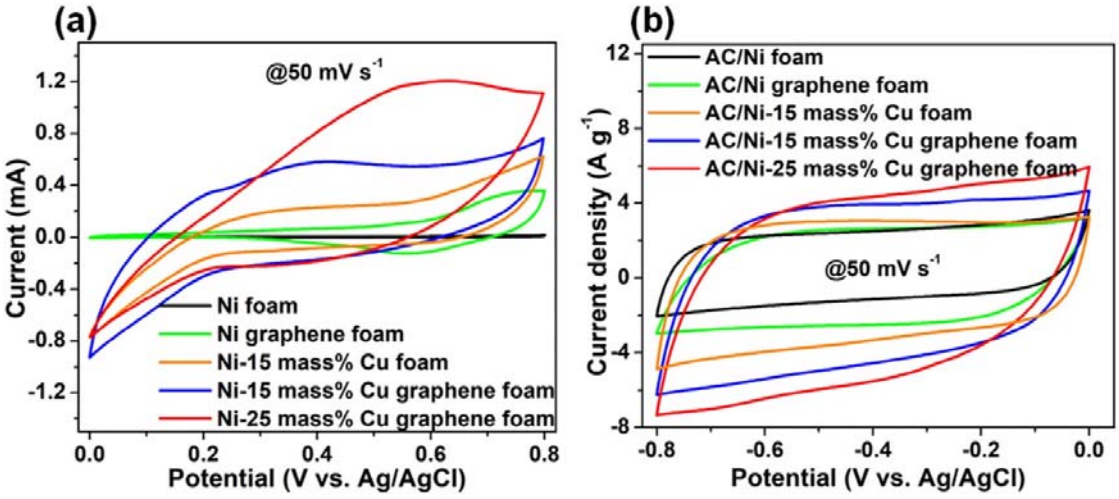

Fig. 7. CV curves of the current collectors (a) without the active material and (b) with the active material at a scan rate of 50 mV s^{-1}.

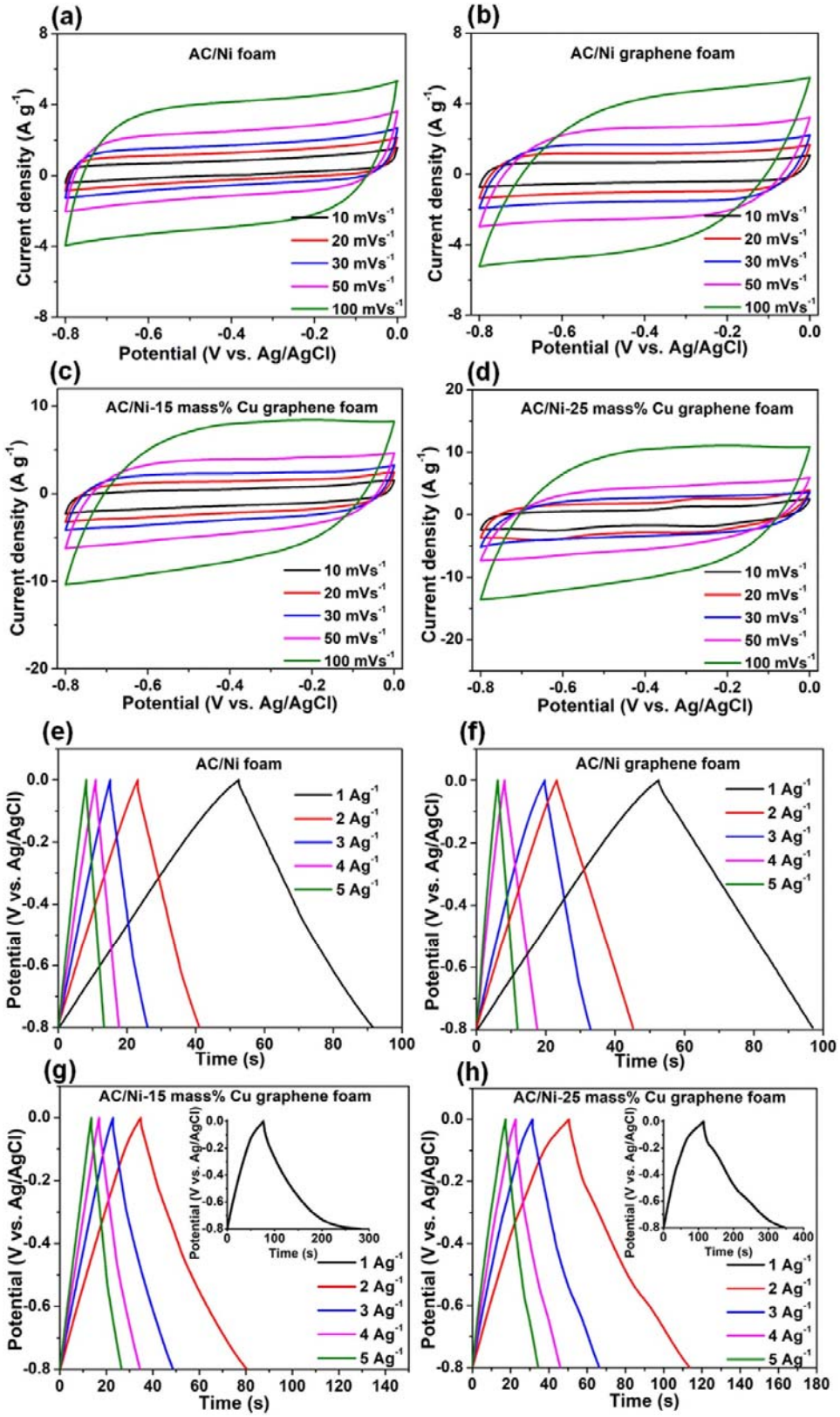

Fig. 8. CV curves at different scan rates of AC on (a) Ni foam (b) Ni graphene foam, (c) Ni-15 mass% Cu graphene foam, (d) Ni-25 mass% Cu graphene foam. GCD plots at different current densities of AC on (a) Ni foam (b) Ni graphene foam, (c) Ni-15 mass% Cu graphene foam, (d) Ni-25 mass% Cu graphene foam.

3.2. Electrochemical characterization

Moreover, the electrochemical performance of the Ni foam, Ni and Ni-Cu graphene foam as current collectors were evaluated in the three-electrode configuration in the negative potential window (−0.8–0.0 V vs. Ag/AgCl) using activated carbon as an active electrode material and 1 M $NaSO_4$ aqueous electrolyte. It is worth mentioning that due to low cost and high availability, the AC electrode materials are the most widely used electrode materials, especially as the negative electrodes. In Fig. 7(a) the CV curves of the current collectors without the active material are shown, to illustrate that Ni foam coated with Cu has a better current response, and with a graphene coating, it has the highest current response. This could be a reason why the electrode material on Ni-Cu graphene foam current collectors exhibits a higher current response, as seen in Fig. 7(b).

Fig. 8(a) to (d) displays the CV curves of the AC on Ni foam, Ni and Ni-Cu graphene foam current collectors evaluated over different scan rates in the range of 10–100 mV s^{-1}. All the CV curves demonstrate a typical electrical double layer capacitor (EDLC) behaviour with its quasi-rectangular characteristic shape which is a feature of porous carbon materials. Fig. 8(e) to (h) presents the GCD curves at different current densities in the range of 1–5 A g^{-1} in the potential window of −0.8–0.0 V vs. Ag/AgCl. The GCD curves display a triangular shape with a linear discharge curve indicating a typical capacitive nature. However, at low current density (1 A g^{-1}), the GCD curves of the AC on Ni-Cu graphene foam current collectors show a longer discharge time than a charging time (Fig. 8(g) and (h) inset figures) which could be due to the capacitance contribution from the current collectors since the ions have enough time to be intercalated/extracted into/out of the electrode during charging/discharging.

Moreover, in agreement with the CV curves (Fig. 7(b)), the GCD curves of the AC on Ni-Cu graphene foam current collectors display a longer discharge time as compared to the electrode material on Ni and Ni graphene foam current collectors (Fig. 9(a)). From the GCD curves the specific capacitance, C_S (shown in Fig. 9(b)) of the electrodes was calculated using the following equation [3,33,34]:

$$C_s = \frac{I\Delta t}{m\Delta V} \tag{1}$$

where I is the current (A), Δt is the discharge time (s), m is the total mass of the active material (g) and ΔV is the potential window (V).

It can be seen from Fig. 9(b) that the AC on Ni-Cu graphene foam current collectors display a higher electrochemical performance in terms of the calculated C_S compared to electrode materials on Ni and Ni graphene foam current collectors. The AC on Ni-25 mass% Cu graphene foam current collector exhibited a high specific capacitance of 289.7 F g^{-1} at a current density of 1 A g^{-1}, and at a high current density of 5 A g^{-1}, the specific capacitance remained as high as 106.7 F g^{-1}. Similarly, the AC on Ni-15 mass% Cu graphene foam current collector exhibited a high specific capacitance of 257.8 F g^{-1} at a current density of 1 A g^{-1}, and at 5 A g^{-1} the specific capacitance remained as high as 81.6 F g^{-1}. The specific capacitance reported in this work for AC (derived from *Quercussuber*) on Ni-Cu graphene foam current collector in 1 M $NaSO_4$ aqueous electrolyte is higher than that reported for ACs (based on various biomass-derived carbons) on Ni foam current collectors and various electrolytes (see Table 2).

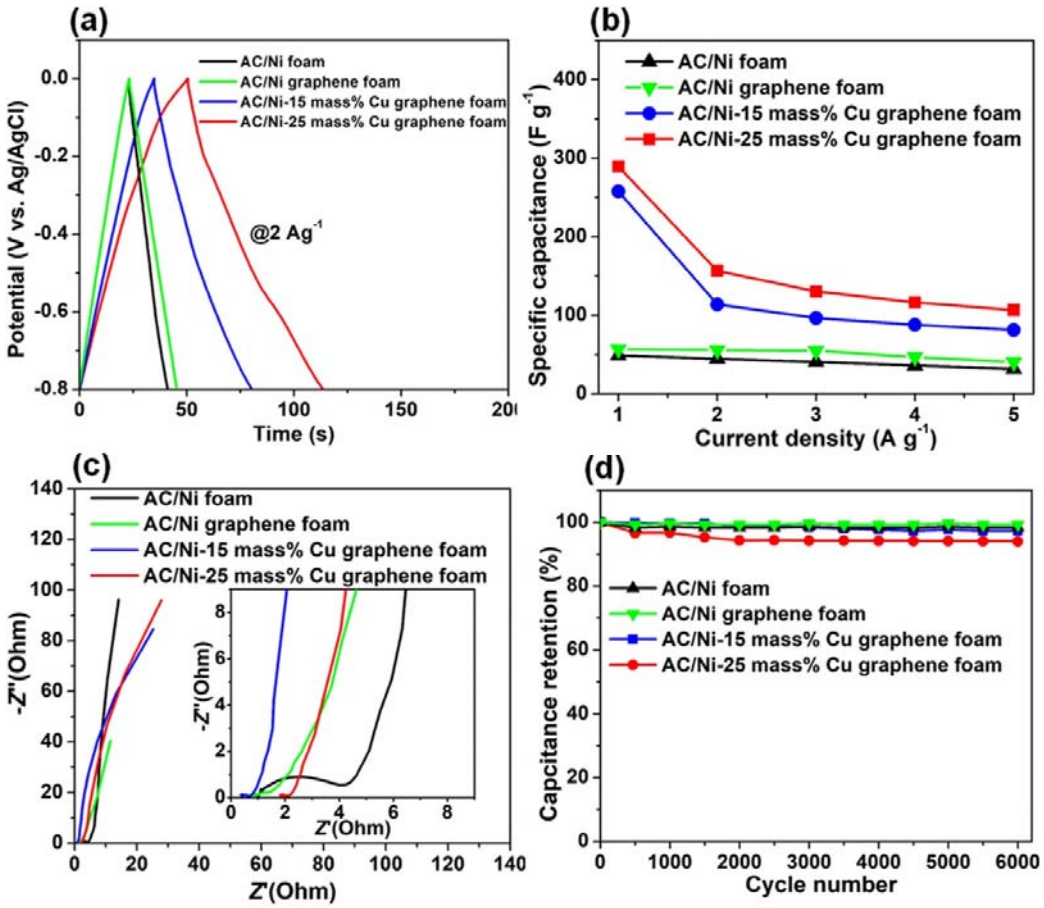

Fig. 9. The electrochemical performance of AC on Ni foam, Ni and Ni-Cu graphene foam current collectors: (a) GCD plots at a current density of 2 A g^{-1}. (b) Specific capacitance as a function of current density. (c) Nyquist plots and (d) capacitance retention over 6000 GCD cycles at 5 A g^{-1}.

Table 2. A comparison of specific capacitances of the reported AC (from various biomass plant) and carbon-based electrode materials on Ni foam current collector and the present work. All values were measured using the three-electrode configuration.

Electrode material/current collector	Electrolyte	Potential window (V)	Current density (A g^{-1})	Specific capacitance (F g^{-1})	Refs.
AC(*Quercussuber*)/Ni-25 mass% Cu graphene foam	1 M Na_2SO_4	−0.8–0.0	1.0	289.7	This work
AC(Quercus Suber)/Ni-15 mass% Cu graphene foam	1 M Na_2SO_4	−0.8–0.0	1.0	257.8	This work
AC(Quercus Suber)/Ni graphene foam	1 M Na_2SO_4	−0.8–0.0	1.0	57.0	This work
AC(Quercus Suber)/Ni foam	1 M Na_2SO_4	−0.8–0.0	1.0	49.1	This work
AC(Quercus Suber)/Ni foam	1 M Li_2SO_4	−1.0–0.0	0.5	105	F. Ochai-Ejeh et al. 2018 [11]
AC(Quercus Suber)/Ni foam	1 M KOH	−1.0–0.0	1.0	102.2	F. Ochai-Ejeh et al. 2017 [12]
AC(Banana peels)/Ni foam	1 M $NaNO_3$	−0.9–0.0	0.5	221	O. Fasakin et al. 2018[13]
AC-Mn_3O_4 /Ni foam	1 M Na_2SO_4	0.0–0.8	0.1	124	K. Makgopa et al. 2017 [14]
[a]OLC-Mn_3O_4 /Ni foam	1 M Na_2SO_4	0.0–0.8	0.1	195	K. Makgopa et al. 2017 [14]
AC(Commercial)/Ni foam	6 M KOH	−1.15–0.0	–	177[b]	I. I. Misnon et al. 2017 [15]
AC(Commercial)/Ni foam	1 M Na_2SO_4	−1.0–0.0	0.8	~100	M. Huang et al. 2014 [16]
AC(Commercial)/Ni foam	1 M Na_2SO_4	−0.8–0.0	–	39[b]	L. Li et al. 2014 [17]
Graphene hydrogel/Ni foam	0.5 M Na_2SO_4	−1.0–0.0	1.0	157.7	H. Gao et al. 2012 [18]
Graphene-Ag/Ni foam	1 M Na_2SO_4	−0.8–0.0	–	210[c]	Y. Shao et al. 2013 [19]

[a] Onion-like carbon (OLC).
[b] Measured from CV at 10 mV s^{-1}.
[c] Measured from CV at ~2 mV s^{-1}.

The electrochemical impedance spectroscopy was further used to evaluate the electrochemical performance of the AC on Ni foam, Ni and Ni-Cu graphene foam current collectors at an open circuit potential, as shown by the Nyquist plots in Fig. 9(c). From this

figure, all the electrodes do not show a semi-circle in the high-frequency region, except for AC on Ni foam (see inset to Fig. 9(c)) which demonstrates a slightly higher electrode-electrolyte interface charge transfer resistance (R_{CT}) of 3.1 Ω. AC on Ni foam, Ni, Ni-15 mass% Cu and Ni-25 mass% Cu graphene foam current collectors display the equivalent series resistance (ESR, i.e. the intersection of the Nyquist plots on the *x*-axis) of 0.94, 0.83, 0.35 and 1.8 Ω, respectively. AC on Ni-15 mass% Cu graphene foam displays less ESR compared to other electrodes and this is due to the alloying of Ni foam with Cu and graphene coating. However, for AC on Ni-25 mass% Cu graphene foam current collector, a high ESR could be due to the high oxygen content in the current collector surface which oxidized a fraction of Ni-Cu alloy into metal oxides with poor electrical conductivity but high redox reactivity which could have contributed to the high capacitance of this electrode. Furthermore, the vertical part of the Nyquist plots (in the low-frequency) with angles >45° could be attributed to resistance due to the diffusion of the fast ions, which resulted in the deviation from the ideal capacitive trend. From the vertical part of the plots, it can be seen that all the electrodes exhibit similar diffusion path length except for AC on Ni graphene foam. Good electrochemical stability (94–100% capacitance retention) for AC on Ni foam, Ni and Ni-Cu graphene foam current collectors was recorded over 6000 constant charge-discharge cycles (Fig. 9(d)).

4. Conclusion

In this work, the Ni-Cu foam alloys were prepared using a three-dimensional (3D) scaffold template of polycrystalline nickel foam which is commonly used as a current collector in supercapacitor electrodes. After that, graphene was grown on Ni and Ni-Cu foam substrates by AP-CVD. The characterization of as-grown Ni and Ni-Cu graphene foam revealed that Ni-Cu graphene foam is mainly monolayer and bilayer as compared to Ni graphene foam which is typically few-layer graphene. The electrochemical properties of as-grown graphene foam samples as current collectors were evaluated in a three-electrode electrochemical cell in the negative potential window using an aqueous electrolyte and activated carbon as active electrode material. The active electrode material coated on Ni-Cu graphene foam current collectors displayed a higher electrochemical performance compared to Ni and Ni graphene foam current collectors. The enhanced electrochemical performance of Ni-Cu graphene foam current collector is mainly due to the synergistic effect between Ni and Cu and the coating graphene sheet. Generally, graphene in electrode materials (or composites) improves capacitance performance and retention life [35,36]. The Ni-Cu graphene foam current collector has the potential to impact on electrochemical performance of supercapacitors.

Author contributions

M.J. Madito: Conceptualization, Methodology, Investigation, Validation and Writing-Original draft preparation. **K.S. Matshoba** (Deceased): Investigation and Validation. **F. U. Ochai-Ejeh:** Investigation. **N. Mongwaketsi:** Investigation. **C.B. Mtshali:** Investigation. **M. Fabiane:** Investigation. **N. Manyala:** Funding acquisition and Resources.

Declaration of competing interest

The authors declare that they have no known competing financial interests or personal relationships that could have appeared to influence the work reported in this paper.

Acknowledgments

This work is based on the research supported by the National Research Foundation (NRF) of South Africa via iThemba LABS Materials Research Department (MRD) and the South African Research Chairs Initiative (SARChI) of the Department of Science and Technology and the NRF.

References

[1] A.S. Lemine, M.M. Zagho, T.M. Altahtamouni, N. Bensalah, Graphene a promising electrode material for supercapacitors—a review, *Int. J. Energy Res*. 42 (2018) 4284–4300, https://doi.org/10.1002/er.4170.

[2] X. Rui, H. Tan, Q. Yan, Nanostructured metal sulfides for energy storage, *Nanoscale*. 6 (2014) 9889, https://doi.org/10.1039/C4NR03057E.

[3] P. Simon, Y. Gogotsi, Materials for electrochemical capacitors, *Nut. Mater*. 7 (2008) 845–854, https://doi.org/10.1038/nmat2297.

[4] J.R. Miller, P. Simon, et al., *Science* 321 (2008) 651–652, https://doi.org/10.1126/science.1158736.

[5] Z.S. Iro, C. Subramani, S.S. Dash, Electrochemical science a brief review on electrode materials for supercapacitor, *Int. J. Electrochem. Sci*. 11 (2016) 10628–10643, https://doi.org/10.20964/2016.12.50.

[6] M. Beidaghi, Y. Gogotsi, Title: Capacitive energy storage in micro-scale devices: recent advances in design and fabrication of micro-supercapacitors capacitive energy storage in micro-scale devices: recent advances in design and fabrication of micro-supercapacitors, *Energy Environ. Sci*. 7 (2014) 867, https://doi.org/10.1039/c3ee43526a.

[7] Y. Wang, A. Du Pasquier, D. Li, P. Atanassova, S. Sawrey, M. Oljaca, Electrochemical double layer capacitors containing carbon black additives for improved capacitance and cycle life, *Carbon N. Y.* 133 (2018) 1–5, https://doi.org/10.1016/J.CARBON.2018.03.001.

[8] C. Liu, J. Liu, J. Wang, J. Li, R. Luo, J. Shen, X. Sun, W. Han, L. Wang, Electrospun mulberry-like hierarchical carbon fiber web for high-performance supercapacitors, *J. Colloid Interface Sci.* 512 (2018) 713–721, https://doi.org/10.1016/J.JCIS.2017.10.093.

[9] A.T. Chidembo, K.I. Ozoemena, B.O. Agboola, V. Gupta, G.G. Wildgoose, R.G. Compton, Nickel(ii) tetra-aminophthalocyanine modified MWCNTs as potential nanocomposite materials for the development of supercapacitors, *Energy Environ*. Sci. 3 (2010) 228, https://doi.org/10.1039/b915920g.

[10] M. Toupin, T. Brousse, D. Be, Charge storage mechanism of MnO 2 electrode used in aqueous electrochemical capacitor, *Chem. Mater.* 16 (2004) 3184–3190.

[11] F. Ochai-Ejeh, M.J. Madito, K. Makgopa, M.N. Rantho, O. Olaniyan, N. Manyala, Electrochemical performance of hybrid supercapacitor device based on birnessite-type manganese oxide decorated on uncapped carbon nanotubes and porous activated carbon

nanostructures, *Electrochim. Acta*. 289 (2018) 363–375, https://doi.org/10.1016/J.ELECTACTA.2018.09.032.

[12] F.O. Ochai-Ejeh, M.J. Madito, D.Y. Momodu, A. Khaleed, O. Olaniyan, N. Manyala, High performance hybrid supercapacitor device based on cobalt manganese layered double hydroxide and activated carbon derived from cork (Quercus suber), *Electrochim. Acta*. 252 (2017) 41–54, https://doi.org/10.1016/j.electacta.2017.08.163.

[13] O. Fasakin, J.K. Dangbegnon, D.Y. Momodu, M.J. Madito, K.O. Oyedotun, M.A. Eleruja, N. Manyala, Synthesis and characterization of porous carbon derived from activated banana peels with hierarchical porosity for improved electro-chemical performance, *Electrochim. Acta*. 262 (2018), https://doi.org/10.1016/j.electacta.2018.01.028.
[14] K. Makgopa, K. Raju, P.M. Ejikeme, K.I. Ozoemena, High-performance Mn3O4/ onion-like carbon (OLC) nanohybrid pseudocapacitor: unravelling the intrinsic properties of OLC against other carbon supports, *Carbon N. Y.* 117 (2017) 20–32, https://doi.org/10.1016/J.CARBON.2017.02.050.

[15] I.I. Misnon, R. Jose, Synthesis and electrochemical evaluation of the PANI/δ-MnO 2 electrode for high performing asymmetric supercapacitors, *New J. Chem*. 41 (2017) 6574–6584, https://doi.org/10.1039/C7NJ00679A.

[16] M. Huang, Y. Zhang, F. Li, L. Zhang, R.S. Ruoff, Z. Wen, Q. Liu, Self-assembly of mesoporous nanotubes assembled from interwoven ultrathin birnessite-type MnO2 nanosheets for asymmetric supercapacitors, *Sci. Rep*. 4 (2014) 3878, https://doi.org/10.1038/srep03878.

[17] L. Li, Z.A. Hu, N. An, Y.Y. Yang, Z.M. Li, H.Y. Wu, Facile synthesis of MnO 2 /CNTs composite for supercapacitor electrodes with long cycle stability, *J. Phys. Chem. C*. 118 (2014) 22865–22872, https://doi.org/10.1021/jp505744p.

[18] H. Gao, F. Xiao, C.B. Ching, H. Duan, High-performance asymmetric supercapacitor based on graphene hydrogel and nanostructured MnO 2, *ACS Appl. Mater*. *Interfaces*. 4 (2012) 2801–2810, https://doi.org/10.1021/am300455d.

[19] Y. Shao, H. Wang, Q. Zhang, Y. Li, High-performance flexible asymmetric super-capacitors based on 3D porous graphene/MnO 2 nanorod and graphene/Ag hybrid thin-film electrodes, *J. Mater. Chem. C.* 1 (2013) 1245–1251, https://doi.org/10.1039/C2TC00235C.

[20] X. Cao, Y. Shi, W. Shi, G. Lu, X. Huang, Q. Yan, Q. Zhang, H. Zhang, Preparation of novel 3D graphene networks for supercapacitor applications, *Small*. 7 (2011) 3163–3168, https://doi.org/10.1002/smll.201100990.

[21] X.C. Dong, H. Xu, X.W. Wang, Y.X. Huang, M.B. Chan-Park, H. Zhang, L.H. Wang, W. Huang, P. Chen, 3D graphene-cobalt oxide electrode for high-performance supercapacitor and enzymeless glucose detection, ACS Nano. 6 (2012) 3206–3213, https://doi.org/10.1021/nn300097q.

[22] T.M. Masikhwa, M.J. Madito, D. Momodu, A. Bello, J.K. Dangbegnon, N. Manyala, High electrochemical performance of hybrid cobalt oxyhydroxide/nickel foam graphene, *J. Colloid Interface Sci*. 484 (2016), https://doi.org/10.1016/j.jcis.2016.08.069.

[23] A. Bello, K. Makgopa, M. Fabiane, D. Dodoo-Ahrin, K.I. Ozoemena, N. Manyala, Chemical adsorption of NiO nanostructures on nickel foam-graphene for supercapacitor applications, *J. Mater. Sci.* 48 (2013) 6707–6712, https://doi.org/10.1007/s10853-013-7471-x.

[24] A.C. Ferrari, D.M. Basko, Raman spectroscopy as a versatile tool for studying the properties of graphene, *Nat. Nanotechnol*. 8 (2013) 235–246, https://doi.org/10.1038/nnano.2013.46.

[25] L.M. Malard, M.A. Pimenta, G. Dresselhaus, M.S. Dresselhaus, Raman spectroscopy in graphene*, Phys. Rep.* 473 (2009) 51–87.

[26] M.J. Madito, N. Manyala, A. Bello, J.K. Dangbegnon, T.M. Masikhwa, D.Y. Momodu, A wafer-scale Bernal-stacked bilayer graphene film obtained on a dilute Cu (0.61 at% Ni) foil using atmospheric pressure chemical vapour deposition, *RSC Adv*. 6 (2016) 28370–28378, https://doi.org/10.1039/C5RA27159B.

[27] L. Liu, H. Zhou, R. Cheng, W.J. Yu, Y. Liu, Y. Chen, J. Shaw, X. Zhong, Y. Huang, X. Duan, High-yield chemical vapor deposition growth of high-quality large-area AB-stacked bilayer graphene, *ACS Nano*. 6 (2012) 8241–8249.

[28] M.S. Yoo, H.C. Lee, S. Lee, S.B. Lee, N.S. Lee, K. Cho, Chemical vapor deposition of bernal-stacked graphene on a Cu surface by breaking the carbon solubility symmetry in Cu foils, *Adv. Mater*. 29 (2017) 1–8, https://doi.org/10.1002/adma.201700753.

[29] M.J. Madito, A. Bello, J.K. Dangbegnon, C.J. Oliphant, W.A. Jordaan, T.M. Masikhwa, D.Y. Momodu, N. Manyala, Raman analysis of bilayer graphene film prepared on commercial Cu(0.5 at% Ni) foil, *J. Raman Spectrosc*. 47 (2016), https://doi.org/10.1002/jrs.4848.

[30] C. Mattevi, H. Kim, M. Chhowalla, A review of chemical vapour deposition of graphene on copper, *J. Mater. Chem*. 21 (2011) 3324.

[31] A. Dato, V. Radmilovic, Z. Lee, J. Phillips, M. Frenklach, Substrate-free gas-phase synthesis of graphene sheets 2008, *Nano Lett*. 8 (2008) 2012–2016.

[32] J.-C. Dupin, D. Gonbeau, P. Vinatier, A. Levasseur, Systematic XPS studies of metal oxides, hydroxides and peroxides*, Phys. Chem. Chem. Phys*. 2 (2000) 1319–1324, https://doi.org/10.1039/a908800h.

[33] B. Akinwolemiwa, C. Peng, G.Z. Chen, Redox electrolytes in supercapacitors, *J. Electrochem. Soc.* 162 (2015) A5054–A5059, https://doi.org/10.1149/2.0111505jes.

[34] A. Laheäär, P. Przygocki, Q. Abbas, F. Béguin, Appropriate Methods for Evaluating the Efficiency and Capacitive Behavior of Different Types of Supercapacitors, (2015), https://doi.org/10.1016/j.elecom.2015.07.022.

[35] H. Wang, Q. Hao, X. Yang, L. Lu, X. Wang, A nanostructured graphene/polyaniline hybrid material for supercapacitors, Nanoscale. 2 (2010) 2164, https://doi.org/10.1039/c0nr00224k.

[36] M. Yu, Y. Huang, C. Li, Y. Zeng, W. Wang, Y. Li, P. Fang, X. Lu, Y. Tong, Building three-dimensional graphene frameworks for energy storage and catalysis, *Adv. Funct. Mater*. 25 (2015) 324–330, https://doi.org/10.1002/adfm.201402964.